PhotoniX

RESEARCH

Open Access

Large-scale optical switches by thermo-optic waveguide lens

Tao Chen[1†], Zhangqi Dang[1†], Zeyu Deng[1†], Shijie Ke[1], Zhenming Ding[1] and Ziyang Zhang[1*]

†Tao Chen, Zhangqi Dang and Zeyu Deng contributed equally to this work.

*Correspondence: zhangziyang@westlake.edu.cn

[1] Laboratory of Photonic Integration, School of Engineering, Westlake University, 18 Shilongshan Road, Hangzhou, China

Abstract

Optical switches are desired in telecom and datacom as an upgrade to electrical ones for lower power consumption and expenses while improving bandwidth and network transparency. Compact, integrated optical switches are attractive thanks to their scalability, readiness for mass production, and robustness against mechanical disturbances. The basic unit relies mostly on a microring resonator or a Mach–Zehnder interferometer for binary "bar" and "cross" switching. Such single-mode structures are often wavelength / polarization dependent, sensitive to phase errors and loss-prone. Furthermore, when they are cascaded to a network, the number of control units grows quickly with the port count, causing high complexity in electronic wiring and drive circuit integration. Herein, we propose a new switching method by thermo-optic waveguide lens. Essentially, this multimode waveguide forms a square law medium by a pair of heater electrodes and focuses light within a chip by robust 1×1 imaging. A 1×24 basic switch is demonstrated with 32 electrodes and only two are biased at a time for a chosen output. By two-level cascading, the switch expands to 576 ports and only four electrodes are needed for one path. The chips are fabricated on wafer scale in a low-budget laboratory without resorting to foundries. Yet, the performance goes beyond state of the art for low insertion loss, low wavelength dependence and low polarization dependence. This work provides an original, alternative, and practical route to construct large-scale optical switches, enabling broad applications in telecom, datacom and photonic computing.

Keywords: Optical switches, Photonic integrated circuits, Optical waveguide, Thermo-optic effect, Square law medium

Introduction

The fast-growing optical communication [1, 2] and photonic computing [3] technologies have propelled the development of large-scale optical switches with small footprint, fast speed, and low power consumption. Switches based on micro-electromechanical systems (MEMS) have been well developed and made their way to commercial devices thanks to the mature micromachining technology on silicon [4–6]. However, in a MEMS switch, light path is essentially steered by the mechanical movement of micro mirrors, which often requires extra calibration and stabilization system against vibration. Though their performance is excellent, the implementation of MEMS switches is hindered by high cost, relatively bulky size, and sensitivity to environmental disturbances.

On the other hand, photonic integrated circuits (PICs) have witnessed tremendous development over the years as the “core” in high-speed transceiver modules, addressing the exponentially growing demand on the optical communication bandwidth in telecom, datacom, and beyond [7, 8]. PIC-based optical switches are compact chips relying on local index change to alter the light path without any moving parts. They can be readily made using a variety of structures on a mature waveguide platform, the most popular of which are microring resonators (MRRs) [9, 10] and Mach–Zehnder interferometers (MZIs) [11, 12]. The MRR switch consists of a ring resonator sandwiched between a pair of waveguides. By changing the local refractive index on the ring, light of the selected wavelength is tuned on and off resonance, resulting in a hopping light path between the drop and through ports. Thanks to the high-quality factor of the ring, such switches can have very sharp spectral widths, and therefore need only minimal power to induce the small index change for on–off switching. The advantage is that the MRR switches can achieve high speed under a compact size and low power consumption. However, the disadvantage is that they work around separate resonant wavelengths and require critical environmental control to stabilize the spectrum for a consistent switching performance over time [13].

To work in a broad band, avoiding the complexity with wavelength channel allocations, the MZI structure is more commonly adopted in large-scale switching networks [14–20]. The basic MZI switch is essentially a 2×2 port device. Light from one input is split into two branches, one goes through a tunable phase shifter, and depending on this extra phase change, the recombined light forms constructive interference at one of the two output ports, completing the switching process. Compared to the MRR structure, the MZI switch is usually more robust against environmental disturbances. However, the problem arises when the MZI units are cascaded to provide more access ports. For instance, a 1×2^{N} network would require (2^{N}-1) units, with N being the cascade level number. When the port number gets large, the design and integration of the electronic drive circuits become challenging [21]. Though a single MZI is relatively insensitive to phase error compared to the high-quality-factor MRR, a large network of MZIs often runs into thermal crosstalk issues and needs feedback circuits to monitor the phase shift and correct the errors adaptively, thereby increasing the complexity and cost of the system [22]. Due to these challenges, the reported large-scale networks have been restricted to 8×8 for the MRR structure [23] and 32×32 for the MZI structure [15–18], to the best of our knowledge.

In this work, a new type of large-scale optical switch is proposed and demonstrated as shown in Fig. 1a. This switch comprises essentially only a multimode waveguide, steered by a set of thermal electrodes. We show by theoretical derivations that the heat generated by biasing the electrodes can create a parabolic refractive index distribution in the waveguide cross-section, as indicated in Fig. 1b and c. This special type of index distribution is called square law medium and was shown to fulfil the function of a perfect lens [24]. One example is the gradient index optical fiber, which has found applications beyond optical communication as mini lenses (GRIN lenses) or collimators [25]. Another example is the wavefront tuning device in a silicon nitride waveguide array, where the geometry of each waveguide is designed to provide an effective

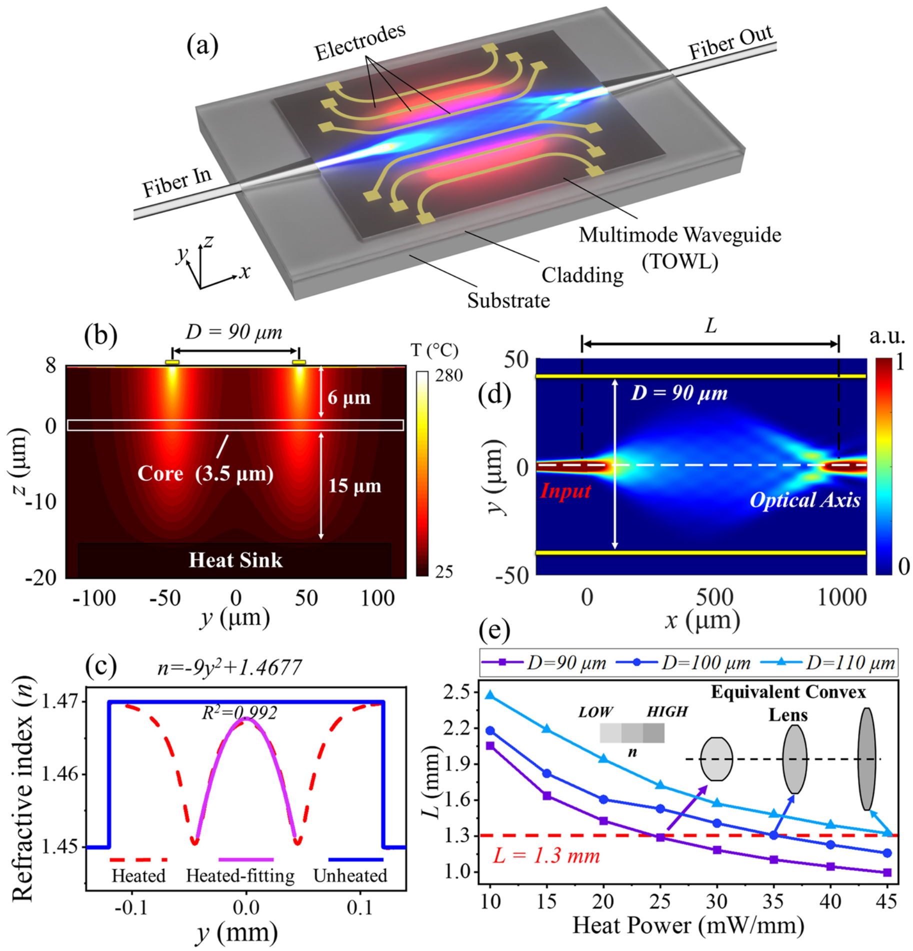

Fig. 1 **a** Layout of the thermo-optic waveguide lens (TOWL). **b** Temperature gradient created by turning on a pair of parallel electrodes spaced over a distance (*D*) of 90 μm, each with a heating power of 45 mW/mm. **c** The resulting refractive index distribution in the waveguide center plane ($z = 0$), forming a parabolic curve along *y*, i.e., a square law medium. **d** The corresponding light focusing behavior in TOWL along the propagation direction *x*. **e** The variation of the 1×1 imaging length *L*, equivalent to 4*f*, under different apertures *D* and heating powers *P*, allowing TOWL to work as an on-chip tunable lens

index point on the parabolic curve, and therefore the entire array works in a similar way as a GRIN lens, but on a chip [26].

Nevertheless, the square law medium reported so far can only provide the function as a fixed lens, with little room for tunability. Here, we report, for the first time to our best knowledge, that the square law medium can be readily formed through thermo-optic effect on a planar waveguide and the "lens" properties can be flexibly tuned by choosing different electrode pairs and with variable heating powers. We show that these changes are equivalent to varying the optical axis, the lens aperture (*D*) and the focal length (*f*) in an imaging system. We call this device thermo-optic waveguide lens (TOWL).

Essentially, TOWL can refocus the input light to different single-mode output waveguides through the 1×1 imaging, or 4*f* effect, by choosing the matched electrode pairs with respective powers, as exemplified in Fig. 1d and e. The imaging effect is experimentally verified on a multimode waveguide with an array of electrodes and an open chip facet to monitor the variation of the near-field light profile via an external lens-camera system, as summarized in Fig. 2. Since the multimode waveguide is relatively wide, it allows an array of output waveguides to be connected, breaking the binary switching limitation from MRR or MZI-based switches. In Fig. 3, we demonstrate a 1×24 switch. With increasing port number, e.g., from 1 to 24, the multimode waveguide gets only slightly expanded in transverse direction, making room for extra electrodes and output waveguides to be placed.

Furthermore, a 1×576 switch is developed by cascading the 1×24 switches in just two levels. As light propagates in the multimode waveguide without sharp boundaries, the edge-roughness induced scattering loss common to single-mode waveguides is avoided. No crossing is needed in the 1×576 switch. The transmission measurement has shown a record low loss for such a device from 1500 to 1600 nm under both transverse

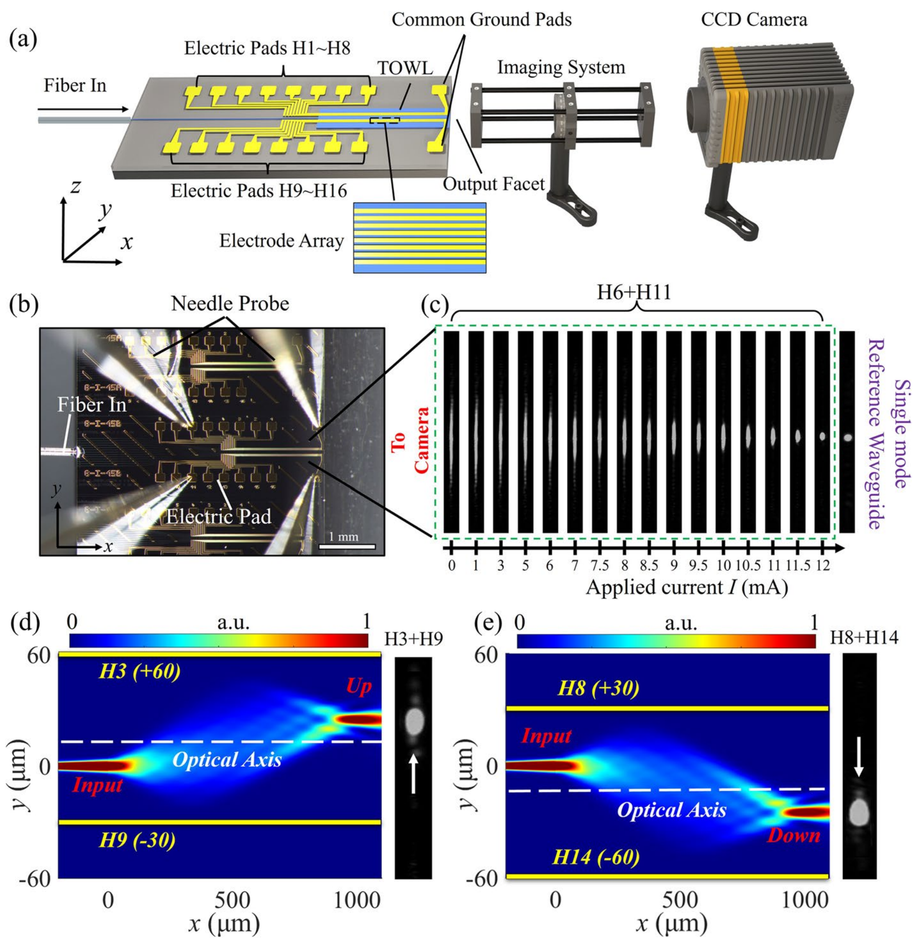

Fig. 2 **a** The experimental setup to monitor the imaging effect of TOWL. **b** The photo of the TOWL chip with an open multimode waveguide facet. **c** The captured near-field intensity profile for the electrode pair H6 + H11 under different heating currents. The center line of the parallel electrodes H6 + H11 is considered as the optical axis of the lens and is aligned with the input waveguide for the on-axis imaging ($y = 0$). **d** The simulation and experimental results show the TOWL driven by the electrode pair H3 + H9, where the optical axis is shifted to $y = +15$ μm. Correspondingly, the off-axis imaging has resulted in a focused spot at $y = +30$ μm. **e** The results under the electrode pair H8 + H14, where the optical axis is shifted to y = -15 μm. Correspondingly, the off-axis imaging has resulted in a focused spot at y = -30 μm

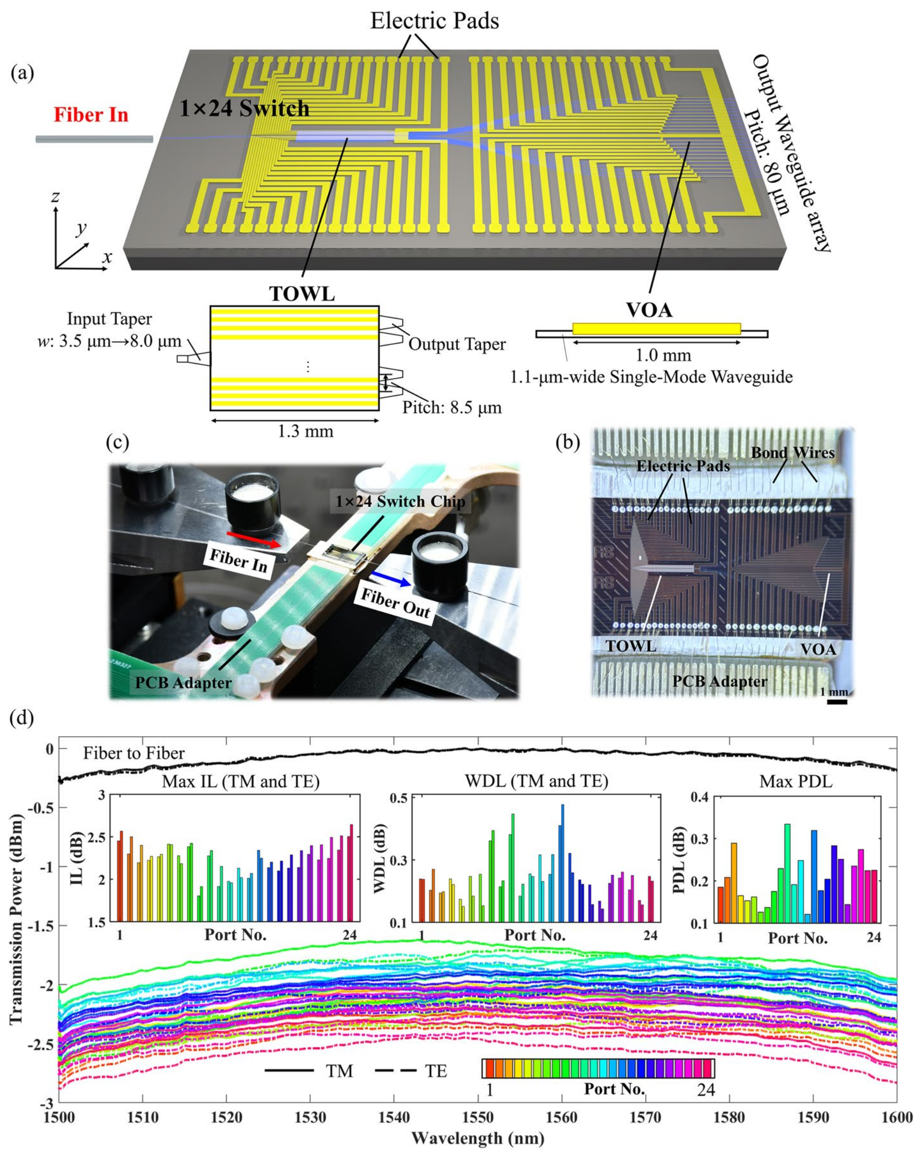

Fig. 3 **a** Layout of the 1 × 24 optical switch. **b** Photo of the chip wire-bonded to the PCB adapter. **c** Photo of the assembly under test. **d** Absolute transmission spectra (in dBm) for all the 24 ports on the chip and the fiber-to-fiber reference without the chip

electric (TE) and transverse magnetic (TM) polarizations after a detailed comparison to the state of the art. The required number of tuning units / electrodes is also significantly lower. Prospects for further development are made at the end.

Methods

Considering the TOWL structure in Fig. 1a, the electrodes on the upper cladding produce a temperature gradient on the cross-section of the multimode waveguide. This temperature distribution can be readily calculated using numerical tools, as displayed in Fig. 1b. Fundamentally, in a solid medium the steady state heat transport equation is denoted by:

$$-\nabla \cdot (k\nabla T) = Q, \tag{1}$$

where k is the thermal conductivity in a unit of W/(m·K), and Q is the applied heat energy transfer rate (W/m^3). Typically, in a planar lightwave circuit the waveguide allows multimode only in the y direction while remaining single mode in the vertical z direction. The core thickness is small, i.e., 3.5 μm in the chosen polymer waveguide platform [27]. The temperature gradient is weak across the modal area in the z direction and can be ignored. Whereas in the y direction the waveguide extends to several tens of micrometers, the modes experience significant temperature / index transition. When considering only the y direction, the heat transfer equation can be simplified to:

$$-k\frac{\partial^2 T}{\partial y^2} = Q \tag{2}$$

For a thermo-optic material, the thermo-optic coefficient c is defined by:

$$c = \frac{dn}{dT} \tag{3}$$

Within a certain temperature range, c can be considered as a constant. The updated refractive index $n(y)$ after heating can be expressed as:

$$n(y) = n_0(y) + c[T\left(y\right) - T_0], \tag{4}$$

where n_0 is the refractive index at room temperature T_0. The heat transfer equation Eq. (2) is then converted to:

$$\frac{\partial^2 n(y)}{\partial y^2} = -c\frac{Q}{k} \tag{5}$$

The general solution to Eq. (5) follows a parabolic form:

$$n = \alpha y^2 + \beta y + \gamma, \tag{6}$$

where α, β, and γ are constants, depending on c, Q, k and the boundaries conditions.

The mathematical derivation above lays the theoretical ground to prove that a square-law medium can be created via a simple thermo-optic effect in a planar waveguide, making it possible to focus light periodically, similar to a gradient index fiber. The simulation result in Fig. 1c verifies this, where the induced refractive index curve follows near to perfect parabolic form. In the chosen polymer waveguide platform, the thermo-optic coefficient is a negative value. Therefore, a pair of electrodes should be adopted to mimic the effect of a convex lens. In positive thermo-optic materials such as silica, the effect can be obtained by applying a single electrode.

Figure 1d shows the light propagation in the multimode waveguide along x by numerical simulation, when D is set to 90 μm and a heating power P to 45 mW/mm on each electrode. The calculated imaging distance L (4*f*) is 1 mm. As only 1×1 imaging is explored in this work, we take the imaging distance L as the main parameter for the rest of this article instead of the equivalent focal length f. Figure 1e summarizes the simulation results showing the variation of L when D and P vary.

The important finding in Fig. 1e is that by choosing proper D and P values, the multimode waveguide can provide the same imaging length L, as indicated by the red dashed line. This means for off-axis imaging the images can be aligned along the y axis at the same x location. Detailed simulations for the off-axis imaging are shown in Fig. S1 in the supplementary document. For off-axis imaging, the image point shifts toward smaller x values with increasing y. In all cases, the images are elongated along x, allowing tolerant coupling to the output waveguide. This is the fundamental ground for designing an optical switch where the output waveguides can be placed along y in response to the shift of the optical axis from different combinations of electrode pairs, starting at the same location in x. It resembles a convex lens in free space, i.e., by varying the curvature (in relation to D) and the index contrast (in relation to P), the lens can provide the same focal length. With TOWL, the lens can be conveniently adjusted on a compact chip by turning on different electrode pairs and giving them different powers. Nevertheless, for far off-axis imaging, it is more efficient to connect the output waveguide at the real focus point. For further work, a curved facet to connect the output waveguides is expected to reduce the loss for the boundary ports.

Next, we verify the imaging effect experimentally. A multimode waveguide chip with an array of 16 parallel electrodes (H1-H16) is chosen for the test, as sketched in Fig. 2a. The input is a tapered waveguide to reduce the junction loss. The multimode waveguide is 1.3 mm long (in x) and 300 μm wide (in y), though the effective width is defined by the electrode pair distance D. The output is an open facet of the multimode waveguide, allowing the examination of the near field profile through an external lens-camera system. Standard single-mode fiber is attached to the input facet and the electrode pair H6 + H11 ($D = 90$ μm) are contacted by needle probes. This pair of electrodes has a central axis (optical axis) at $y = 0$, i.e., the same location of the input waveguide. A photo of the chip in measurement is shown in Fig. 2b. The electrodes are injected with identical current for symmetric operation.

Figure 2c displays the transition of the near field profile at the multimode waveguide output facet with increasing current. When the electrodes are unbiased, the original light intensity profile is of a prolonged Gaussian shape, similar to beam broadening in a slab waveguide. This profile becomes gradually narrowed with increasing current. At 12 mA, the profile reaches the smallest, focused spot. The intensity profile from a single mode waveguide placed on the same chip is displayed as a reference.

After confirming the focusing effect, another set of electrodes is chosen, i.e., H3 + H9. The center of the parallel electrode pair defines the optical axis, and this combination is equivalent to moving the optical axis up to $y = +15$ μm. With the object (input waveguide) located at $y = 0$, the inverse image should appear at $y = +30$ μm. This is confirmed by both simulation and experiment, as shown in Fig. 2d. Symmetrically, by tuning on the electrode pair H8 + H14, the image is shifted down to $y =$ -30 μm, as verified in Fig. 2e. This allows an array of output waveguides to be connected at the multimode waveguide facet, while the input stays at the fixed location. By varying the combination of electrode pairs, light can be switched to different output ports. This is the working principle behind the TOWL optical switches.

Results

Following the principle, a 1×24 optical switch is constructed by adjoining 24 output waveguides on the multimode waveguide facet, as sketched in Fig. 3a. In total 32 electrodes are added, some of which can be reused for neighboring ports by allowing a small variation of D and asymmetrical heating powers. The output waveguides follow a fan-out structure to an array with a pitch of 80 µm, intended for a reduced-cladding fiber array (RC-FA) to be attached. Though the TOWL itself has a small footprint of 1.3 mm in x and 0.24 mm in y, sufficient space is given to the waveguide fan-out, considering the pitch size and the large bending radius (3 mm) for the low-index contrast polymer waveguide (1.47:1.45). At the output side, each waveguide is accompanied by an offset electrode ranging from 400 µm on the side ports to 1 mm in the middle. This compact and simple design fulfils the function of a variable optical attenuator (VOA) in order to suppress the inter-channel crosstalk [28]. With contact pads suitable for an in-house wire bonding facility and reference waveguides for alignment assistance, the chip measures 8.5 mm in x and 4.5 mm in y.

The output port count 24 is chosen under the considerations of thermal threshold for the material, the insertion loss and crosstalk. Since the degradation temperature of the chosen polymer starts at 300 °C, we allow a maximum heating power $P = 45$ mW/mm, equivalent to a local temperature of 255 °C. Under this limitation, the parabolic index distribution can be kept for an aperture $D \leq 110$ µm. The minimal imaging length ($L = 4f$) is determined to be 1.3 mm. The width of the input and output tapers is set to 8.0 µm to suppress the junction coupling loss. To avoid severe crosstalk, the gap between the output tapers is set to 0.5 µm. Finally, as both sides of the input port can be used to create TOWL, the allowed number of the output ports can be calculated as $2 \times (110/8.5-1) \approx 24$.

In this work, we choose to work on polymer waveguides because polymer materials possess both relatively large thermo-optic coefficient and low thermal conductivity, which are beneficial to develop highly efficient thermally tunable devices. The fabrication follows a standard process on a 4-inch silicon wafer using conventional contact lithography (SUSS MA6) and reactive ion etching [27]. After dicing, the chip is electrically wire bonded to a PCB adapter, as show in Fig. 3b. The adapter is then connected via a bus cable to a homemade circuit board capable of providing up to 64 current sources. The integration and characterization technology are inherited from the function programmable waveguide engine (FPWE) [29]. The photo of the chip under test is shown in Fig. 3c.

The input light from a tunable laser (EXFO T100S-HP) is injected into the chip with a standard single-mode fiber (Corning SMF-28e). This laser is equipped with a polarization control unit capable of generating 6 polarizations, though only linearly polarized TE and TM lights are chosen for the wavelength scan. The output fiber of the same type is fed to the detector system (CT-440). The transmission spectra are recorded for both polarizations from 1500 to 1600 nm. At first, fiber-to-fiber measurement is performed as the reference, labelling the system loss. The chip is then placed, aligned to the fiber pair, and the currents on the selected electrode pair are adjusted via a computer program. The characterization results are summarized in Fig. 3d, where the solid and dashed lines indicate the TM and TE polarizations, respectively.

It is worth noting that in Fig. 3d, the spectra are recorded as absolute transmitted power in dBm, where the total insertion loss (IL) includes fiber-chip coupling losses at both facets and waveguide propagation loss throughout the chip. The insets analyze the loss characteristics of the 24 ports in detail, referencing to the fiber-to-fiber transmission, i.e., the black curves on the top. The IL spectrum can be obtained by simply subtracting the fiber-to-fiber reference from the transmission of a chosen channel. The boundary ports suffer from higher loss than the ports in the middle, due to image distortion from the aberration effect for larger off-axis distances. The maximal (worst) IL among all ports is 2.6 dB, occurring at port 24 for TE polarization at 1600 nm, whereas for port 9 the maximal IL is as low as 1.7 dB for the TM polarization at 1600 nm. The best result happens for port 9 under TM polarization at 1545 nm, where the IL is merely 1.5 dB. For any of the 24 ports, the wavelength dependent loss (WDL) is below 0.5 dB and the polarization dependent loss (PDL) is smaller than 0.4 dB.

To dissect the loss contribution, the fiber-chip coupling loss is suppressed to below 0.3 dB by inversely tapering the waveguide to a tip of 1.1 μm, thereby enlarging the mode profile similar to that of a single-mode fiber [28]. The propagation loss of a single-mode polymer waveguide is below 1 dB/cm, obtained by the standard cut-back measurement on waveguides of the same design but different lengths. Both fiber-chip coupling loss and waveguide propagation loss show little polarization dependence. As light propagates in the multimode waveguide under a parabolic index profile upon heating, the light field does not experience the edge roughness arising from reactive ion etching when defining the waveguide structure. Therefore, the sidewall scattering loss typical to step-index waveguide is avoided in TOWL.

To analyze the crosstalk, we have chosen two ports in the middle, i.e., #14 and #18, as well as the two side ports #24 and #1. The neighboring channels (± 1) are measured when the TOWL switch is set to work on the target port. The second neighboring channels (± 2) all feature a low crosstalk below -30 dB. The results are displayed in Fig. 4. When the VOA is not activated, the switch exhibits a relatively large crosstalk and in the worst situation, it goes up to -13.1 dB (targeted at #18, measured at #17, TE polarization, at 1500 nm). This is attributed to the unwanted coupling at the multimode waveguide end-facet to the output waveguide array. When the VOA electrode is switched on, the crosstalk can be suppressed to below -30 dB for all the ports tested under both polarizations from 1500 to 1600 nm.

Following the excellent performance of the TOWL device, we go on forward and design a 1×576 switch by cascading the 1×24 switches in two levels. The layout is shown in Fig. 5a. To make the chip compact, the output ports are organized into three groups along the north, east, and south sides of the chip. The pitch is set to 80 μm, allowing RC-FAs to be attached to the three facets. The chip measures 4.7 cm from north to south and 3 cm from east to west. A photo is shown in Fig. 5b. In total 800 electrodes are placed on the chip, while only four are needed to define one path.

It requires tremendous effort to cover the measurement for all the 576 ports. Instead, we have selected the following ports as representatives for proof of concept: on the east side #12 [2, 7, 13, 16, 20, 23] and #13 [1, 4, 11, 16, 21, 24]; on the south side #24 [1, 4, 7, 9, 11, 16, 20, 24]. The first number following the # sign indicates the port number on the 1×24 switch of the first level. The numbers in the brackets are the ports measured on

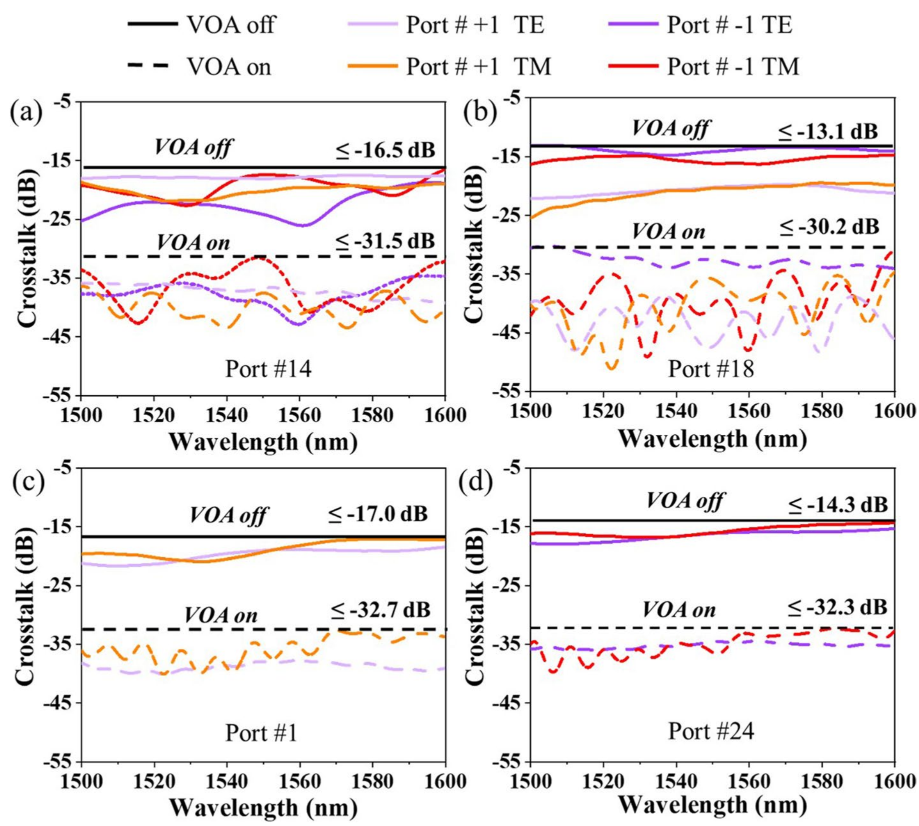

Fig. 4 The crosstalk characterization on the neighboring ports adjacent to the target port **a** #14, **b** #18, **c** #1 and **d** #24. The solid lines indicate the crosstalk without activating the on-chip VOA, where the worst crosstalk is lower than -13.1 dB. The dashed lines are the measurement when the respective VOA is turned on, where the crosstalk level is suppressed below -30 dB regardless of polarization and for all wavelengths

the respective 1×24 switches of the second level. The results for the east side measurement are summarized in Fig. 5c and for the south side in Fig. 5d.

Since the polymer waveguide features a low index contrast and therefore requires a relatively large bending radius (3 mm), the majority of the loss comes from the single-mode waveguides for interconnect. This is manifested by the higher loss from the chosen ports on the east side than on the south side. Though the wavelength and polarization dependent waveguide losses are weak, they become prominent when the waveguides extend to centimeters long. Nevertheless, when confined within the C-band (from 1530 to 1565 nm), this switch features an IL below 7.8 dB, a WDL below 0.5 dB, and a PDL below 0.6 dB for all the 20 ports measured under both polarizations.

Discussions

The self-imaging principle in a step-index multimode waveguide was long discovered and the multimode interference devices (MMIs) have been developed for beam splitting but also as the critical 90° hybrid in a coherent receiver [30, 31]. However, in a step-index MMI, the self-imaging effect takes place for a chosen input at discrete x and y locations. When the input moves along the waveguide facet in y, the imaging effect deteriorates abruptly. This is fundamentally different in TOWL, where the input (object) can shift

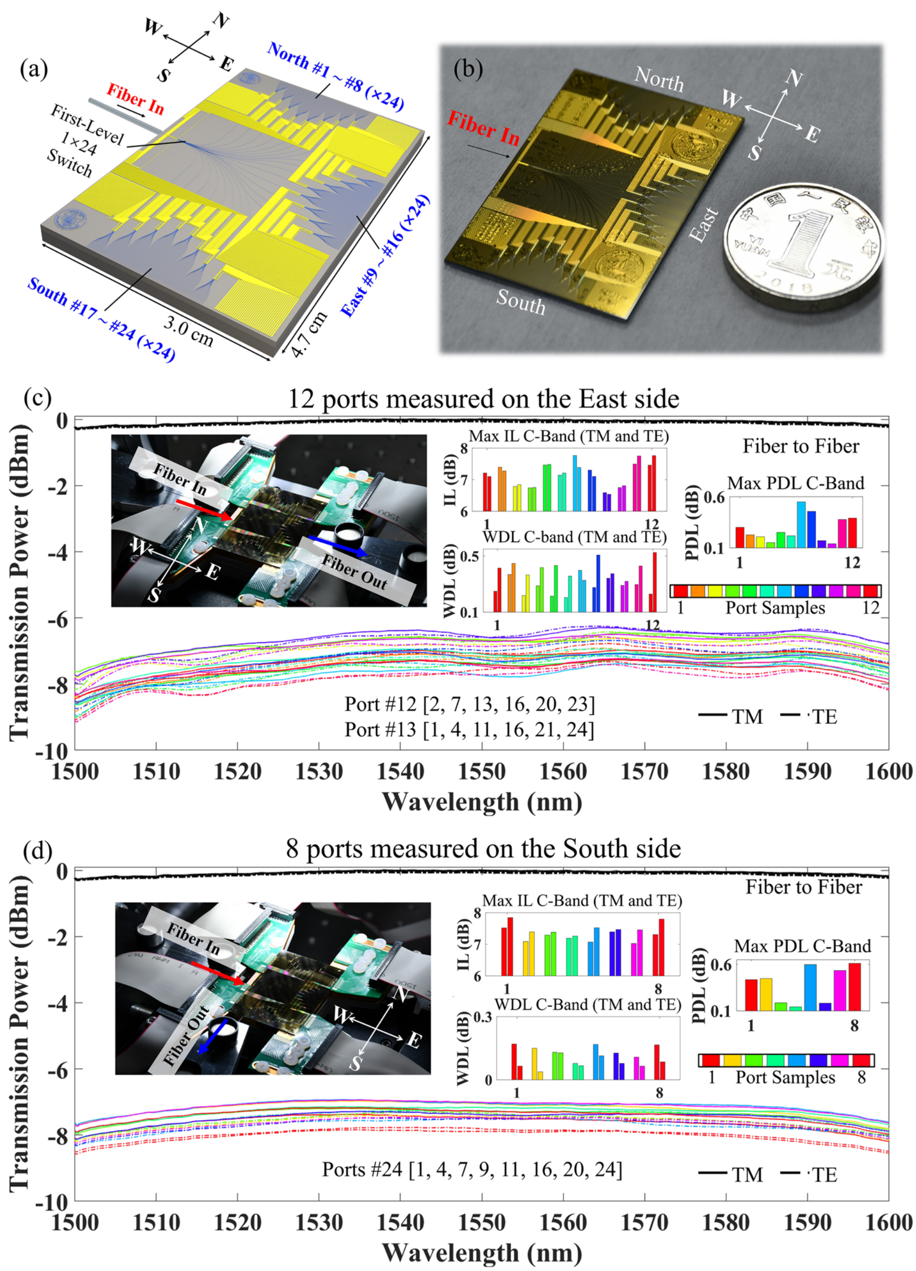

Fig. 5 **a** Layout and **b** photo of the 1 × 576 optical switch. **c** Absolute transmission spectra (in dBm) for the chosen 12 ports on the east side of the chip. **d** Absolute transmission spectra (in dBm) for the chosen 8 ports on the south side of the chip

along the y axis, so long as paraxial approximation holds, and the output (image) moves in the opposite direction in y following the 1 × 1 inverse imaging principle. The comparison is summarized in Fig. S2 in the supplementary document. Detailed analysis regarding the individual and collective mode behavior between conventional step-index MMI and TOWL will be covered in our future work.

As a new type of switch, TOWL shows excellent performance compared to the existing single-mode-based switches. The comparison to the state of the art is given in

Table 1. Detailed comparison regarding the topology of the MZI and TOWL switches when building a large-scale network is given in Fig. S3 and Table S1 in the supplementary document. In particular, to construct a 1×1024 switching network, the MZIs need to be cascaded in 10 levels, requiring in total 1023 units. As in practice two electrodes are needed to drive one MZI, the number of electrodes goes up to 2026. For each path, 20 electrodes need to be turned on simultaneously. For the TOWL switch, by doubling the 1×576 structure reported in this work, e.g., with a simple 1×2 switch placed on the first level, the port number goes up to 1×1152. In total 1602 electrodes should be placed and 6 are needed for one path. Future work includes the exploration on the limit of the port number (beyond 24) that a single TOWL can hold without cascading, in terms of waveguide index contrast, thermo-optic coefficient and maximal allowed work temperature. To further reduce the electrode number, asymmetrical heating can be applied, and the image point can be shifted effectively by the same electrode pair. In our future work, the coverage of each electrode and the overlap capability will be studied in detail to draw the theoretical guidelines for the electrode layout with a minimal electrode number. As a thermally tunable device, the response time of the TOWL switch is on the millisecond level. Nevertheless, by careful driver electrode design, electro-optic effect, e.g., in lithium niobate, should also be able to generate a parabolic index profile, making it possible to develop ultrafast electro-optic waveguide lenses (EOWLs).

Though only one input port is given in this first demonstration, the TOWL can well expand to $N \times N$ ports and fulfill switching functions under strictly blocking, conditional

Table 1 Comparison of large-scale integrated optical switches

Refs	Year	Port Count	Switch Type and Materials	IL (dB)	XT (dB)	Polarization PDL (dB)	λ range (nm) WDL (dB)	Footprint (mm^2) and Power
[14]	2016	16×16	EO-MZI Silicon	~20 on-chip	-10	TE only	1530 ~ 1590 not given	10.7×4.4 1.17 W
[15]	2017	32×32	EO-MZI Silicon	24.3 on-chip	-14.1	TE only	1500 ~ 1570 7.1	12.1×5.2 max 542.3 mW
[16]	2018	32×32	TO-MZI Silicon	~ 45 on-chip	~-22	TE only	1530 ~ 1565 not given	12×12 < 1 W (on-die)
[17]	2019	32×32	TO-MZI Silicon	12.8 1547 nm f2f	-20	TE only	1547 (14.2 nm bandwidth for -20 dB XT)	10×26 1.9 W
[18]	2020	32×32	TO-MZI SiN/Si	~65 f2f	-13.1	TE and TM ~ 7	demonstrated at 1547	22.5×10 not given
[19]	2001	1×128	TO-MZI Silica	4.3 f2f	-29.8	not given	not given	57×60 max 3.2 W
[32]	2012	1×100	TO-Phase Array InP	15.2 on-chip	-50	TE only	1533 ~ 1570 3	6×6.5 < 25 mW
This work	2024	1×576	TOWL Polymer	8.9 f2f	< -30	TE and TM 0.81	1500 ~ 1600 1.9	30×47 ~ 0.5 W

The IL, XT, PDL values are given for the worst cases

EO electro-optic, *TO* thermo-optic, *IL* insertion loss, *XT* crosstalk, *PDL* polarization dependent loss, *WDL* wavelength dependent loss, *f2f* fiber to fiber nonblocking and strictly nonblocking scenarios, as sketched in Fig. S4 in the supplementary document. The conditional nonblocking structure is of particular interest as it features the same size as the $1 \times N$ switch, adding the input waveguide array on the front facet of the multimode section. Like a conventional lens, TOWL allows multiple beams to be imaged. These beams, however, all follow the same imaging principle and cannot be routed to arbitrary ports individually. Nevertheless, unlike the physical waveguide crossing, the beam crossing within a TOWL does not generate extra loss and can be explored for on-chip beam steering applications.

Conclusions

To summarize, a new optical switching method is proposed and verified first by theoretical derivations that reveal the underlying physics to generate the square law medium. This thermo-optic waveguide lens (TOWL) behaves as a tunable lens by heating different pairs of parallel electrodes placed above the waveguide. Simulations and experiments have verified that the aperture and the focal length of the lens can be effectively altered, for on-axis as well as off-axis 1×1 imaging. This lens effect is used to construct compact 1×24 and further 1×576 optical switches with low insertion loss and low polarization dependence across a wide wavelength range. The switches show superior performance over the literature, yet requiring less electrodes to operate, leading to a relaxed electric integration technology.

Without resorting to expensive foundries, the fabrication follows a standard process on a 4-inch silicon wafer in a low-budget cleanroom using conventional equipment with minimal feature size above 1 μm. The silicon wafer used in this work serves as a mechanical base and a heat sink, without optical and electrical functions. Though demonstrated on polymer waveguides as proof of concept, the TOWL technology can well be transferred to other platforms so long as thermo-optic effect is present and the thermal conductivity is low. As the chosen polymer materials feature a negative thermo-optic coefficient, a pair of electrodes is needed to lower the index on the sides for the effect of a convex lens. On a glass waveguide, only one electrode is required for the same effect owing to the positive sign of the thermo-optic coefficient. In silicon, however, the high thermal conductivity tends to create a uniform temperature upon heating and therefore it is difficult to generate an index gradient efficiently for TOWL operation.

As future work, in addition to the further miniaturization of the TOWL layout and optimization of the performance, the aberration effect should be studied, as the images start to deteriorate for the far off-axis ports. This can be solved by terminating the multimode waveguide with a curved facet, allowing different imaging lengths for the boundary ports. In addition, as the electrodes can be flexibly placed, an array of heaters may create an index distribution of merged parabolas, allowing complex lens groups to be implemented for advanced on-chip imaging experiments.

Abbreviations

EO	Electro-optic
EOWL	Electro-optic waveguide lens
FPWE	Function programmable waveguide engine
IL	Insertion loss
MEMS	Micro-electromechanical system
MMIs	Multimode interference devices

MRR	Microring resonator
MZI	Mach-Zehnder interferometer
PCB	Printed circuit board
PDL	Polarization dependent loss
PIC	Photonic integrated circuit
RC-FA	Reduced-cladding fiber array
TE	Transverse electric
TM	Transverse magnetic
TO	Thermo-optic
TOWL	Thermo-optic waveguide lens
VOA	Variable optical attenuator
WDL	Wavelength dependent loss
XT	Crosstalk

Supplementary Information

The online version contains supplementary material available at https://doi.org/10.1186/s43074-024-00131-w.

Supplementary Material 1.

Acknowledgements
The authors would like to thank the industry partners for their sincere support and many valuable discussions.
The authors acknowledge Mr. Hao Wei from the China Academy of Art for his help in the figure art design.

Authors' contributions
TC, ZQD and ZZ proposed the idea, completed the theoretical analysis and prepared the manuscript. ZMD and ZZ completed the chip fabrication. TC, ZMD, ZYD and SK performed the experiments. ZZ supervised the overall projects. All the authors analyzed the data and discussed the results. All the authors read and approved the final manuscript before submission.

Funding
This research received no external funding.

Availability of data and materials
The calculation and experiment data that support the works of this study are available from the corresponding authors on reasonable request.

Declarations

Competing interests
The authors declare that they have no competing interests.

Received: 31 January 2024 Revised: 28 March 2024 Accepted: 10 April 2024
Published online: 18 April 2024

References

1. Cheng Q, Rumley S, Bahadori M, Bergman K. Photonic switching in high performance datacenters. Opt Express. 2018;26(12):16022–43.
2. Wu B, Zhang W, Zhou H, Dong J, Huang D, Wai PKA, et al. Chip-to-chip optical multimode communication with universal mode processors. PhotoniX. 2023;4(37):1–14.
3. Zhou H, Dong J, Cheng J, Dong W, Huang C, Shen Y, et al. Photonic matrix multiplication lights up photonic accelerator and beyond. Light Sci Appl. 2022;11(1):30.
4. De Dobbelaere P, Falta K, Gloeckner S, Patra S. Digital MEMS for optical switching. IEEE Commun Mag. 2002;40(3):88–95.
5. Mizukami M, Yamaguchi J, Nemoto N, Kawajiri Y, Hirata H, Uchiyama S, et al. 128×128 three-dimensional MEMS optical switch module with simultaneous optical path connection for optical cross-connect systems. Appl Opt. 2011;50(21):4037–41.
6. Cao T, Hu T, Zhao Y. Research status and development trend of MEMS switches: a review. Micromachines. 2020;11(7):694.
7. Wang Z, Xu J, Yang P, Wang Z, Duong LHK, Chen X. High-radix nonblocking integrated optical switching fabric for data center. J Lightwave Technol. 2017;35(19):4268–81.
8. Wang C, Zhang D, Yue J, Lin H, Zhang X, Zhang T, et al. On-chip optical sources of 3D photonic integration based on active fluorescent polymer waveguide microdisks for light display application. PhotoniX. 2023;4(13):1–15.
9. Wang F, Wang X, Zhou H, Zhou Q, Hao Y, Jiang X, et al. Fano-resonance-based Mach-Zehnder optical switch employing dual-bus coupled ring resonator as two-beam interferometer. Opt Express. 2009;17(9):7708–16.
10. Cheng Q, Dai LY, Abrams NC, Hung Y-H, Morrissey PE, Glick M, et al. Ultralow-crosstalk, strictly non-blocking microring-based optical switch. Photonics Res. 2019;7(2):155–61.

11. Watts MR, Sun J, DeRose C, Trotter DC, Young RW, Nielson GN. Adiabatic thermo-optic Mach-Zehnder switch. Opt Lett. 2013;38(5):733–5.
12. Kita T, Mendez-Astudillo M. Ultrafast silicon MZI optical switch with periodic electrodes and integrated heat sink. J Lightwave Technol. 2021;39(15):5054–60.
13. Jayatilleka H, Murray K, Guillén-Torres MÁ, Caverley M, Hu R, Jaeger NA, et al. Wavelength tuning and stabilization of microring-based filters using silicon in-resonator photoconductive heaters. Opt Express. 2015;23(19):25084–97.
14. Lu L, Zhao S, Zhou L, Li D, Li Z, Wang M, et al. 16 × 16 non-blocking silicon optical switch based on electro-optic Mach-Zehnder interferometers. Opt Express. 2016;24(9):9295–307.
15. Qiao L, Tang W, Chu T. 32 × 32 silicon electro-optic switch with built-in monitors and balanced-status units. Sci Rep. 2017;7(1):42306.
16. Dumais P, Goodwill DJ, Celo D, Jiang J, Zhang C, Zhao F, et al. Silicon photonic switch subsystem with 900 monolithically integrated calibration photodiodes and 64-fiber package. J Lightwave Technol. 2018;36(2):233–8.
17. Suzuki K, Konoike R, Hasegawa J, Suda S, Matsuura H, Ikeda K, et al. Low-insertion-loss and power-efficient 32 × 32 silicon photonics switch with extremely high-Δ silica PLC connector. J Lightwave Technol. 2019;37(1):116–22.
18. Suzuki K, Konoike R, Yokoyama N, Seki M, Ohtsuka M, Saitoh S, et al. Nonduplicate polarization-diversity 32 × 32 silicon photonics switch based on a SiN/Si double-layer platform. J Lightwave Technol. 2020;38(2):226–32.
19. Watanabe T, Goh T, Okuno M, Sohma Si, Shibata T, Itoh M, et al., editors. Silica-based PLC 1 × 128 thermo-optic switch. Proceedings 27th European Conference on Optical Communication (Cat No 01TH8551). Amsterdam: IEEE; 2001. p. 134–5.
20. Gao W, Li X, Lu L, Liu C, Chen J, Zhou L. Broadband 32 × 32 strictly-nonblocking optical switch on a multi-layer Si_3N_4-on-SOI platform. Laser Photonics Rev. 2023;17(11):2300275.
21. Suzuki K, Konoike R, Matsuura H, Matsumoto R, Inoue T, Namiki S, et al., editors. Recent advances in large-scale optical switches based on silicon photonics. Optical Fiber Communication Conference. San Diego: Optica Publishing Group; 2022. p. W4B. 6.
22. Milanizadeh M, Aguiar D, Melloni A, Morichetti F. Canceling thermal cross-talk effects in photonic integrated circuits. J Lightwave Technol. 2019;37(4):1325–32.
23. Huang Y, Cheng Q, Hung Y-H, Guan H, Meng X, Novack A, et al. Multi-stage 8 × 8 silicon photonic switch based on dual-microring switching elements. J Lightwave Technol. 2019;38(2):194–201.
24. Marcuse D. Light propagation in square law medium. In: Light transmission optics 2nd. New York: Van Nostrand Reinhold. 1982. p. 263–285.
25. Gomez-Reino C, Perez MV, Bao C, Flores-Arias MT. Design of GRIN optical components for coupling and interconnects. Laser Photonics Rev. 2008;2(3):203–15.
26. Niu Y, Niu Y, Hu X, Hu Y, Du Q, Yu S, et al. On-chip wavefront shaping in spacing-varied waveguide arrays. Nanophotonics. 2023;12(19):3737–45.
27. Dang Z, Deng Z, Chen T, Ding Z, Zhang Z. C/L-band 2-port broadband wavelength multiplexing switch using polymer waveguides. J Lightwave Technol. 2023;41(8):2451–7.
28. Deng Z, Ding Z, Chen T, Zhang Z. Thermal gradient driven variable optical attenuator with on-chip CNT absorber. IEEE Photonics Technol Lett. 2024;36(4):243–6.
29. Chen T, Dang Z, Ding Z, Liu Z, Zhang Z. Multibit NOT logic gate enabled by a function programmable optical waveguide. Opt Lett. 2022;47(14):3519–22.
30. Soldano LB, Pennings EC. Optical multi-mode interference devices based on self-imaging: principles and applications. J Lightwave Technol. 1995;13(4):615–27.
31. Zhang Z, Maese-Novo A, Polatynski A, Mueller T, Irmscher G, de Felipe D, et al., editors. Colorless, dual-polarization 90 hybrid with integrated VOAs and local oscillator on polymer platform. Optical Fiber Communication Conference. Los Angeles: Optica Publishing Group; 2015. p. Th1F. 3.
32. Soganci IM, Tanemura T, Nakano Y. Integrated phased-array switches for large-scale photonic routing on chip. Laser Photonics Rev. 2012;6(4):549–63.

Publisher's Note